RSC Advances

PAPER

View Article Online
View Journal | View Issue

Cite this: *RSC Adv.*, 2021, **11**, 31448

A new phase transfer nanocatalyst $NiFe_2O_4$–PEG for removal of dibenzothiophene by an ultrasound assisted oxidative process: kinetics, thermodynamic study and experimental design

Fahimeh Vafaee,[a] Mansour Jahangiri *[a] and Masoud Salavati-Niasari *[b]

In this study, $NiFe_2O_4$–PEG, an effective nanocatalyst was synthesized *via* a hydrothermal method using different PEG concentrations and synthesis times. The synthesized nanocatalyst was used in the ultrasound assisted oxidative desulfurization (UAOD) of model fuels (*e.g.* *n*-hexane and dibenzothiophene (DBT)) for the first time. The nanocatalyst was then characterized by XRD, FTIR, BET, SEM, VSM and TEM analyses. In addition, central composite design was used to evaluate the effective variables on the UAOD process. The optimal values of effective factors such as catalyst dose, oxidant amount, irradiation time and ultrasonic power to maximize of the percentage of sulfur removal were 0.149 g, 15 mL, 11.96 min, and 70 MHz, respectively. Moreover, the kinetic aspects of the oxidation reaction of DBT in the UAOD process were investigated using a pseudo-first-order model. Furthermore, using the Arrhenius equation, an activation energy of 35.86 kJ mol^{-1} was obtained. Additionally, thermodynamic analysis showed that the oxidation reaction of DBT was endothermic with a positive Gibbs free of energy, indicating the non-spontaneity of oxidation of DBT in the UAOD process. Moreover, the conversion rate of DBT has increased from 57% at 35 °C to 85% at 65 °C.

Received 8th September 2021
Accepted 8th September 2021

DOI: 10.1039/d1ra06751f

rsc.li/rsc-advances

1. Introduction

Liquid fuels consist of various organosulfur compounds such as sulfides, disulfides, thiophenes and their corresponding derivatives. Sulfur is emitted in the form of sulfur dioxide (SO_2) upon burning liquid fuels, which is harmful for human health and the environment as a whole.[1] Therefore, reducing the amount of sulfur has become one of the most important activities of refineries. Different methods such as hydrodesulfurization (HDS) have been used to remove sulfur from hydrocarbon fuels. However, this process is not effective in eliminating BT, DBT and 4,6-DMDBT from fossil fuels.[2,3] Deep HDS is an alternative method for the production of ultra-low sulfur diesel fuel. However, this method requires over a three-fold increase in the catalyst volume/reactor size and harsh reaction conditions, making it extremely expensive.[4–6] Oxidative desulfurization (ODS) is an alternative method for the latter method since it can be performed under mild conditions (low temperature and pressure), is highly selective and does not require the application of expensive hydrogen in the process.[7–9] In ODS, sulfur compounds are oxidized into the corresponding sulfoxides and sulfones *via* the electrophilic addition of oxygen using a catalyst and an oxidizing agent.[10,11] A wide range of oxidants such as hydrogen peroxide,[12] Fenton reagent,[13] ozone[14] and molecular oxygen[15] have been used to oxidize organosulfur compounds to sulfoxides and/or sulfones. One of the most widely used oxidants for the sulfur removal is hydrogen peroxide because of its cheap price, ease of accessibility, and environmentally benign nature.[16,17] However, there are still some drawbacks associated with ODS process including the insolubility of the organosulfur substrate and oxidant, resulting in their reaction merely at the interface. Consequently, the conversion and reaction rates of sulfur compounds are reduced. Therefore, ultrasound technology has been used to increase the efficiency of ODS method.[18–20] The advantage of ultrasound assisted oxidative desulfurization (UAOD) method over ODS is the higher desulfurization rate because ultrasound irradiation is an effective method for enhancing the interfacial area between the fuel and oxidant through the generation of cavitation and microstreaming.[21] In contrast, phase transfer catalysts (PTC) or phase transfer agents (PTA) possessing exceptional capability of dissolution in both organic and aqueous phases have been used in the ODS process.[22] In fact, PTC is used to enhance mass transfer in emulsion systems.[23,24] Collins *et al.*[16] employed PTC for oxidation of sulfur compounds in fuels. Jiarong *et al.*[25] reported that the main problem related to PTC was its recovery in the industry. Therefore, in the present work, attempt has been

[a]*Faculty of Chemical, Petroleum and Gas Eng., Semnan University, P. O. Box 35196-45399, Semnan, Islamic Republic of Iran. E-mail: mjahangiri@semnan.ac.ir*
[b]*Institute of Nano Science and Nano Technology, University of Kashan, P. O. Box. 87317-51167, Kashan, Islamic Republic of Iran. E-mail: salavati@kashanu.ac.ir; Fax: +98 31 55913201; Tel: +98 31 55912383*

Table 1 Levels of factors in response surface design

	Levels		
Factors	−1	0	1
Irradiation time (min), X_1	5	10	15
Oxidant amount (mL), X_2	5	10	15
Catalyst dose (g), X_3	0.05	0.1	0.15
Ultrasonic power (MHz), X_4	30	50	70

made to solve the problem of PTC recovery by using the magnetic property of metal oxides. In addition, significant types of metal oxides are spinel ferrite (SF) magnetic compounds. In this study, phase transfer nanocatalysts of polyethylene glycol have been synthesized and characterized using magnetic nickel ferrite. $NiFe_2O_4$–PEG has also been prepared by hydrothermal method with different concentrations of PEG during various reaction times. In addition, the effects of catalyst amount, irradiation time, amount of oxidant and ultrasound frequency on the DBT oxidation in the UAOD process were investigated. The kinetic and thermodynamic properties of dibenzothiophene oxidation including ΔH°, ΔG° and ΔS° have also been investigated. The model developed by Zhao *et al.*[26] has been used to study the kinetics of the oxidation reaction of DBT in the UAOD process.

2. Experimental section

2.1. Materials

Commercially available chemicals and solvents were used with no further purification. Dibenzothiophene (DBT), *n*-hexane, hydrogen peroxide (H_2O_2 30 vol%), nickel nitrate $Ni(NO_3)_2 \cdot 6H_2O$, ferric nitrate $Fe(NO_3)_3 \cdot 9H_2O$ and polyethylene glycol (PEG 4000) were purchased from Sigma Aldrich Chemical Co.

2.2. Synthesis of the phase-transfer-type (NiF_2O_4–PEG) nanocatlyst

0.2 g of $Ni(NO_3)_2 \cdot 6H_2O$, 0.68 g of $Fe(NO_3)_3 \cdot 9H_2O$ and 0.86 g of carbohydrate (sucrose) were all dissolved in 10 mL of distilled water. The solution (i) obtained was then stirred using a magnetic stirrer to obtain a clear solution. A solution (ii) of PEG was next prepared in two concentrations of (5% and 7%) in distilled water. Afterwards, 10 mL of PEG solution (ii) were added to solution (i). After continuous stirring at 400 rpm for an hour, a homogenous solution was obtained, which was then transferred to a Teflon container and placed in a hydrothermal furnace at 150 °C for different hydrothermal synthesis times (5, 7, and 10 hours). Subsequently, after cooling the sample to room temperature, it was centrifuged and consecutively washed 3 times with distilled water and ethanol, respectively, to remove the impurities. And finally dried in a vacuum oven at 25 °C for 12 h.

2.3. UAOD process of prepared model fuel

The model fuel was obtained by dissolution of dibenzothiophene (DBT) in *n*-hexane to prepare a 200 ppm concentration of sulfur. Appropriate volumes of model fuel with phase transfer type ($NiFe_2O_4$–PEG) nanocatalyst and hydrogen peroxide as oxidizing agent were added into the reaction vessel. The mixture obtained was subjected to ultrasonication (Model HD3400, Bandelin, Germany) for a specific time. The oxidation reaction of DBT was performed in the temperature range of 35° to 65 °C to obtain the activation energy. The ultrasonic probe was

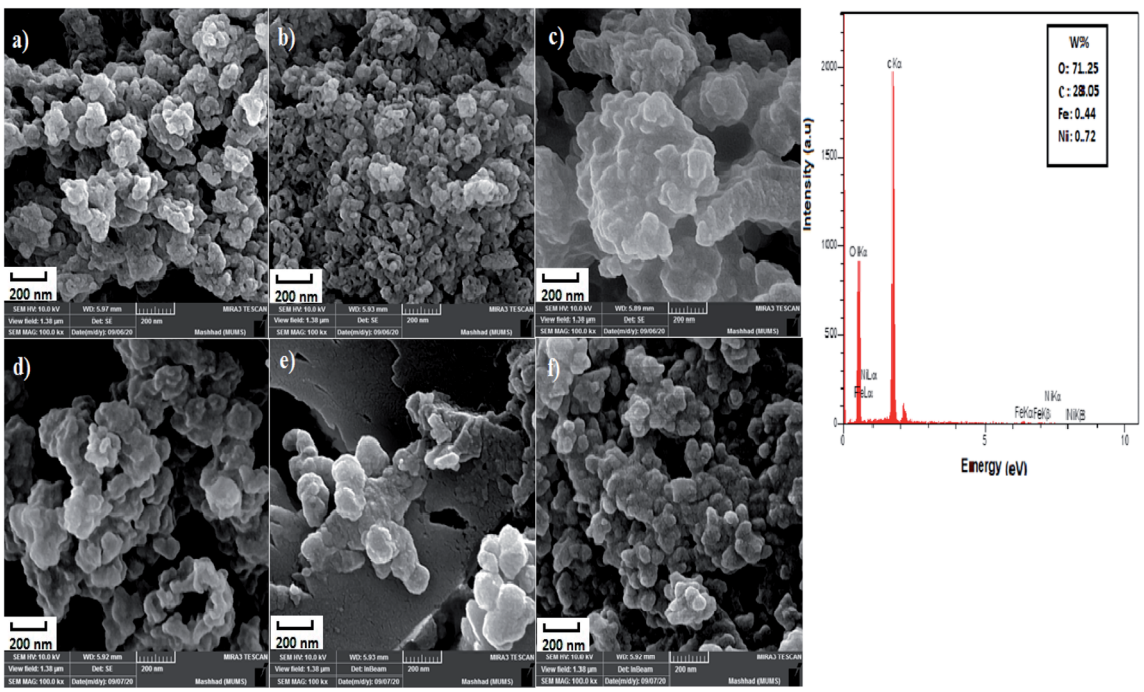

Fig. 1 SEM images of (a–c) $NiFe_2O_4$–7% PEG (5 h, 7 h, 10 h), (d–f) $NiFe_2O_4$–5% PEG (5 h, 7 h, 10 h) in 200 nm and EDS images of $NiFe_2O_4$–7% PEG (10 h).

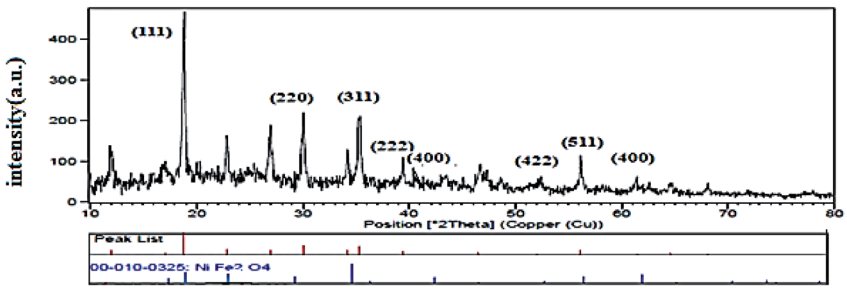

Fig. 2 XRD pattern of $NiFe_2O_4$–7% PEG (10 h).

immersed in the reaction vessel center at three quarters of the solution depth. Ultrasonic intensities were evaluated at different values of 30, 50 and 70 MHz at different time intervals (5, 10 & 15 min). The mixture was then centrifuged after cooling to separate the organic and aqueous phases. Sulfur concentration was measured using a Petro test X-ray fluorescence sulfur meter (Tanaka scientific Ry-360sH), according to ASTM D-42946. The efficiency of the UAOD was calculated using the following equation:

$$\text{UAOD efficiency } (\%) = \left[1 - \frac{S_f}{S_i}\right] \times 100 \quad (1)$$

where S_f and S_i are the final and initial concentrations (mg L^{-1}) of DBT in the solution, respectively.

2.4. Design of experiment

A multi-variable of the response surface design, central composite design (CCD), was used to evaluate the effects of process variables including the catalyst dose, oxidant amount, irradiation time and ultrasonic power on sulfur removal percentage (response), facilitating the data fitting through the quadratic model. The levels of the independent factors were coded as −1, 0 and 1 for low, central or middle, and high points, respectively. Table 1 shows the ranges and levels of the variables

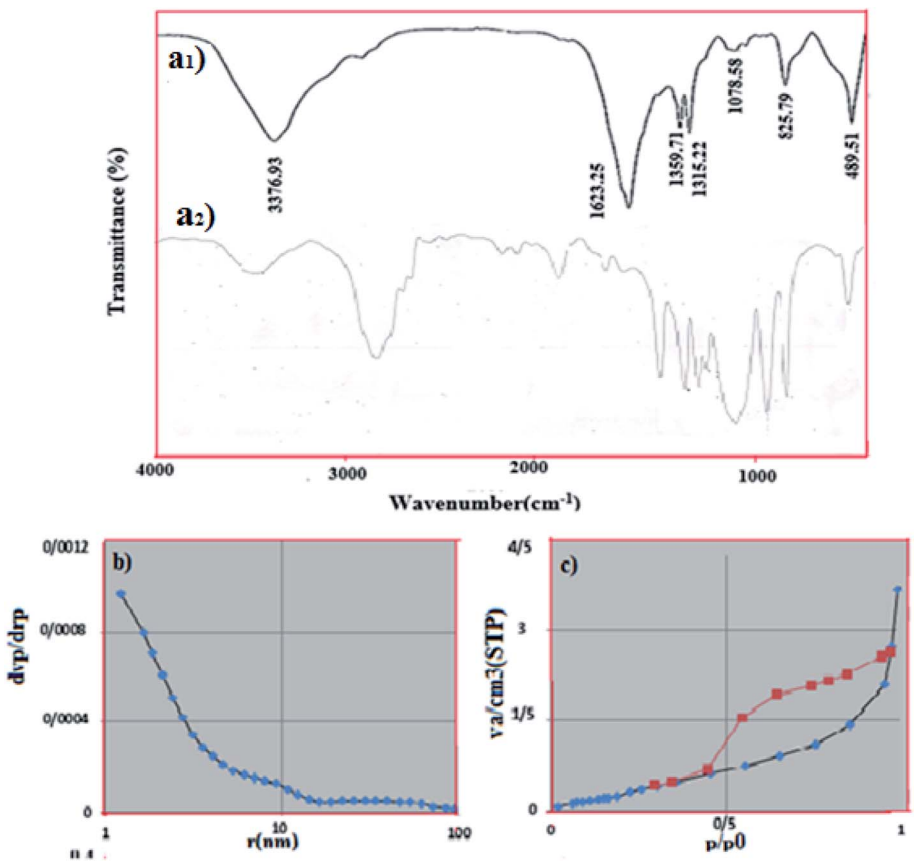

Fig. 3 (a) ((a$_1$) FT-IR spectrum of obtained $NiFe_2O_4$–PEG (a$_2$) pure PEG), (b) N_2 adsorption–desorption isotherm (c) pore size of $NiFe_2O_4$–7% PEG (10 h).

in the coded units based on RSM studies. The experimental data were then evaluated using Minitab 18 (trial version) including ANOVA to determine the responses and interactions between the processed variables. In this work, 25 experiments was carried out to investigate the effects of the four main independent variables including irradiation time (X_1), oxidant amount (X_2), catalyst dose (X_3) and ultrasonic power (X_4) on sulfur removal efficiency.

3. Results and discussion

3.1. Nanocatalyst characteristics

3.1.1. SEM EDS images. SEM was used to determine the microstructure of the synthetic products. The Scanning Electron Microscopy (SEM) images of hybrid nanocatalysts based polyethylene glycol (PEG) with different selected PEG contents are shown in Fig. 1. The SEM images of $NiFe_2O_4$–7% PEG (5 h, 7 h, 10 h) nanocatalysts are shown in Fig. 1(a–c), respectively. The SEM images of $NiFe_2O_4$–5% PEG (5 h, 7 h, 10 h) nanocatalysts are shown in Fig. 1(d–f), respectively. It is clear that all micrographs show two phases in almost good dispersion and high degree of homogeneity. The magnetic phase is arranged or distributed in a circular manner, forcing the other phase to fellow the same trend. It is also observed that as the PEG wt% ratio increases, its density increases in the nanocatalyst and hence the arrangements or the distribution of PEG become better and clearer. In addition, it is clearly observed in the micrographs that the average grain size of PEG increases as its ratio increases. According to the EDS spectrum the presence of Fe, Ni, O and C can confirm the high purity of products.

3.1.2. XRD analysis. The XRD patterns of $NiFe_2O_4$–PEG nanocatalysts, indicating phase type, crystal structure, product purity and the size of crystalline grains. Fig. 2 show the XRD images of $NiFe_2O_4$–7% PEG (10 h). The PEG with a well-defined crystal structure, strong reflection peaks at 19.23° and 23.35° and weak reflection peaks at 26.09°, 35.25° and 38.91° has a high crystalline nature. The crystalline peaks of PEG and nickel ferrite are also observed in the structures of all the related nanocatalysts, which indicates the presence of PEG in the samples. All of the diffraction peaks observed is indexed by the $NiFe_2O_4$ cubic structure of (JCPDS no. 19-629). The line profile, which is shown in Fig. 2, corresponds to the eleven peaks with the following miller indices: (111) (220) (311) (400) (422) (511) (440). Using Scherer equation below, the crystal size of $NiFe_2O_4$ was found to be 53 nm.

$$D = \frac{k\lambda}{\beta \cos \theta} \tag{2}$$

In which D, θ, λ, and FWHM are the size of the crystal, Bragg angle of peaks (°), wavelength (0.154 nm) and full width at half maximum (rad), respectively, and k is a constant equal to 0.89.

3.1.3. FTIR analysis. Fig. 3(a1) shows the FTIR spectra of $NiFe_2O_4$–PEG nanocatalyst in the range of 4000–400 cm^{-1}. It is revealing clear that the broad peaks observed at respectively are attributed to the adsorbed water and PEG, respectively, corresponding which are assigned to the vibration of OH and H–O–H

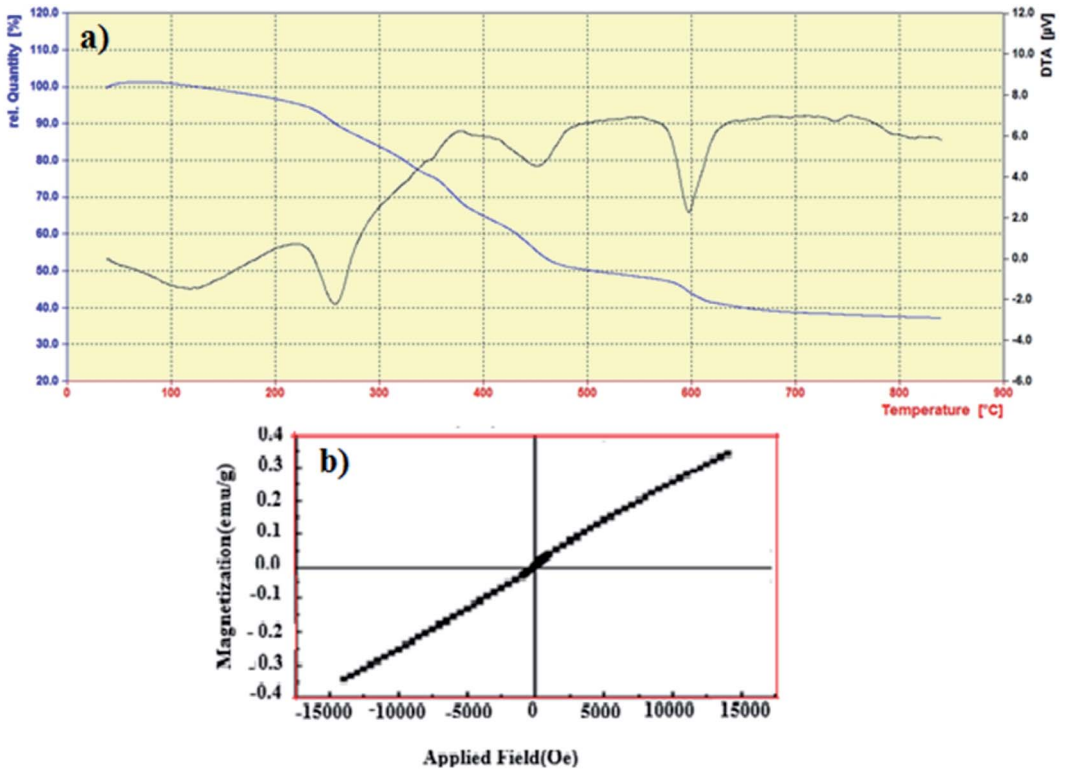

Fig. 4 (a) TGA curve of $NiFe_2O_4$–7% PEG (10 h) (b) VSM curve of $NiFe_2O_4$–7% PEG (10 h) nanocatalyst.

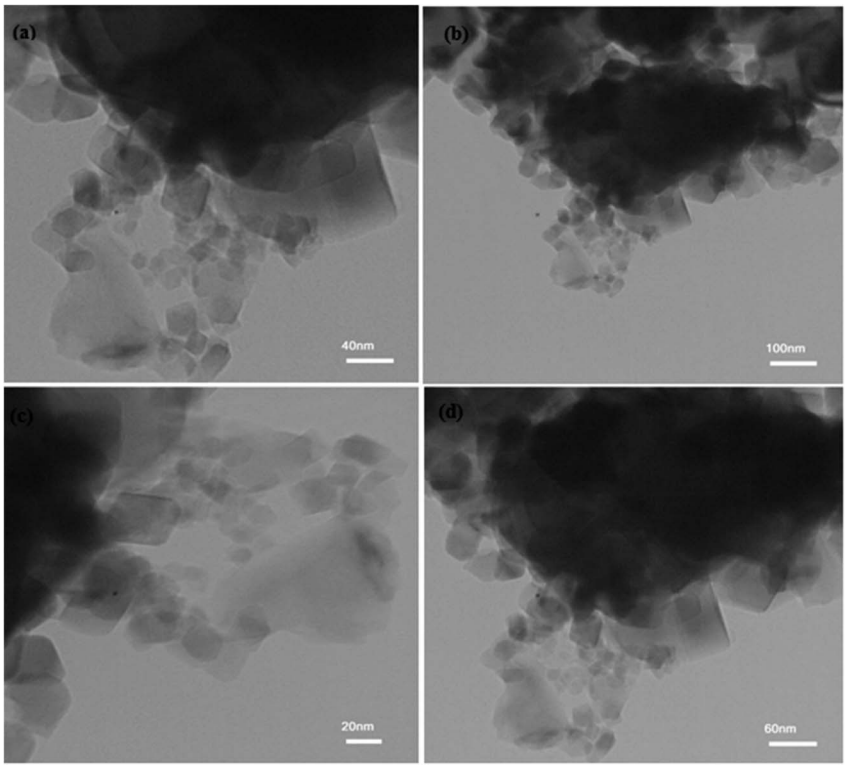

Fig. 5 TEM images of $NiFe_2O_4$–7% PEG (10 h) nanocatalyst in four different scales (a) 40 nm (b) 100 nm (c) 20 nm (d) 60 nm.

groups. The two bands at 825.76 and 489.51 cm^{-1} are attributed to the stretching vibrations of Fe═O and Ni═O, respectively.[27] The intense peak at 3376.93 cm^{-1} and the less intensive one at 1624 cm^{-1} are ascribed to the stretching vibration between hydrogen and oxygen atoms.[28,29] Fig. 3(a2) shows the FTIR spectra of pure PEG, that shows many characteristic peaks at 3423, 2878, 1965, 1648, 1467,1343, 1281, 1243, 1114, 963, 843 and 530 cm^{-1} matching with the reported results.[30,43]

Table 2 Presents a summary of previous literature in oxidative desulfurization with PTA[a]

Sl. no	Authors	Reaction conditions	PTA	Oxidation system	% reduction
1	Sachdeva *et al.*,[45]	DBT (325 ppm); solv.: octane normal; tem.: 70 °C; str.: 1000 rpm	TOAB	H_2O_2/phosphotungstic acid	98
2	Zhao *et al.*,[26]	DBT (600 ppm); solv.: heptane normal; tem.: 45 °C; str.: 200 rpm	TBSB	H_2O_2/CH_3COOH	86.4 thiophene, 97.5 DBT
3	Mei *et al.*,[38]	Thiophene (400 ppm); react vol.: 50 mL; US freq.: 20 kHz; tem.: 75 °C	TOBA	H_2O_2/phosphotungstic acid	98
4	Chen *et al.*,[47]	Thiophene + DBT (960); solv. toluene; tem.: 88 °C; US freq.: 20 kHz	TOAB	H_2O_2/phosphotungstic acid	88.4
5	Wan *et al.*,[48]	DBT + BT + thiophene + 2-methyl-T + 4-methyl-DBT	TOAF TDAB, TOAB, TBAB	H_2O_2/phosphotungstic acid	90.3, 59.9, 43.6, 38.3
6	Rezvani *et al.*,[39]	BT + DBT + 4,6-DMDBT + 4-methyl-DBT (500 ppm); solv.: *n*-heptan; tem; 60 °C; str.: 500 rpm	$(TBA)_4PW_{11}Fe$@pbo	H_2O_2/CH_3COOH	97
7	Rezvani *et al.*,[49]	Gasoline + BT + TH + DBT (500 ppm); react vol.: 50 mL; tem.: 35 °C; str.: 600 rpm	PMOCu–$MgCu_2O_4$@PVA	H_2O_2/CH_3COOH	Gasoline: 97, DBT: 99, BT: 97, TH: 98
9	Cuihong Zhou *et al.*,[50]	Crude oil + gasoline; tem.: 50 °C	—	H_2O_2/HCOOH/PW/ acetonitrile/methanol	Crude oil: 72, gasoline: 81
10	Najafi *et al.*,[51]	Diesel (7240 ppm)	Fe_2SO_4	H_3PO_4/H_2O_2	69
11	Present work	DBT(200 ppm); solv.: *n*-hexane; tem.: 35 °C; US freq.: 70 MHz; react vol.: 40 mL	$NiFe_2O_4$–PEG	H_2O_2	85

[a] TOAB – tetraocthyl ammonium bromide, TBAB – tetrabuthyl ammonium bromide, TBAB – tetrabutyl ammonium bromide, TOBA – tetraoctyl bromide ammonium MBAH – methyltributyl ammonium hydroxide, TODAB – tetraoctadecyl ammonium bromide, TOAF – tetraoctyl ammonium fluoride, TDAB – tetradecyl ammonium bromide. Tem – temperature, vol – volume, str – stirrer speed, US freq – ultrasound frequency.

3.1.4. BET results. The specific surface area of $NiFe_2O_4$–PEG nanocatalyst was determined using Brunauer–Emmett–Teller (BET). Fig. 3(b) shows the corresponding N_2 adsorption/desorption isotherm, which indicates a porous structure (isotherm type IV and H_2-type hysteresis) for this compound. H_2-Type hysteresis loop is associated with porous compounds, based on the IUPAC classification. BET surface area was 2.5001 $m^2\ g^{-1}$. The micropore diameter was found to be 1.21 nm by BJH method (Fig. 3(c)).

3.1.5. TGA analysis. Thermal stability of $NiFe_2O_4$–7% PEG (10 h) nanocatalyst was investigated using TGA analysis in Fig. 4(a) In the TG curve, weight loss of about 28% is observed in the temperature range of 25–800 °C, which is related to the relatively strong bonding force between PEG and Fe_2O_3 nanoparticles, so it can be concluded that PEG is located on the surface of ferrite nickel nanoparticles. It is observed that a small fraction of weight loss from room temperature to 100 °C is related to the evaporation of water absorbed in the sample. In the DTA curve, two weight losses of about 280 and 470 are related to the thermal oxidative decomposition of PEG polymer.[31,32]

3.1.6. VSM analysis. In order to study the effect of PEG on the magnetic behavior of the nanocatalysts prepared, magnetization measurements were performed. Fig. 4(b) shows the magnetic hysteresis loop. The saturation magnetization (Ms) and coercivity (Hc) of the $NiFe_2O_4$ nanoparticles were 0.3428 emu g^{-1} and 14 000 Oe, respectively. Clear hysteresis loops were shown by the magnetization of the samples under the applied field demonstrated due to their ferromagnetic behavior.[30]

3.1.7. TEM images. Fig. 5 shows the TEM images in four different scales. The dark field images exhibit the polyethylene glycol catalyst. On the other hand, the presence of nanocrystals between 100, 60, 40 and 20 nm is observed in bright field mode. TEM analysis shows that the use of PEG has increased the crystallization and reduced the agglomeration of nanoparticles as well as controlling their spherical shape.

3.2. UAOD results of prepared model fuel

The $NiFe_2O_4$–PEG nanocatalysts were synthesized using different amounts of PEG and hydrothermal reaction times. Fig. 6 displays the comparison of the performances of $NiFe_2O_4$–PEG 5% (5 h, 7 h, 10 h) and PEG 7% (5 h, 7 h, 10 h) nanocatalyst in the desulfurization process. Fig. 6 for picted in Fig. 5, $NiFe_2O_4$-7% PEG (10 h) nanocatalyst shows the best performance among all nanocatalysts due to the highest PEG wt% with growth of oxidation of DBT. Furthermore, increasing the hydrothermal synthesis time resulted in the better homogeneity of nickel ferrite particles. A comparison of the nanocatalysts in this work with those reported in the literature is given in Table 2. The literature reports mainly deal with high concentrations (>500 ppm) of sulfur while the least concentration of sulfur (200 ppm) was used in this work. Thus, the nanaocatalysts used in this work showed better efficiencies compared with those reported in the literature because desulfurization of fuels with low sulfur concentrations is difficult (Fig. 6).

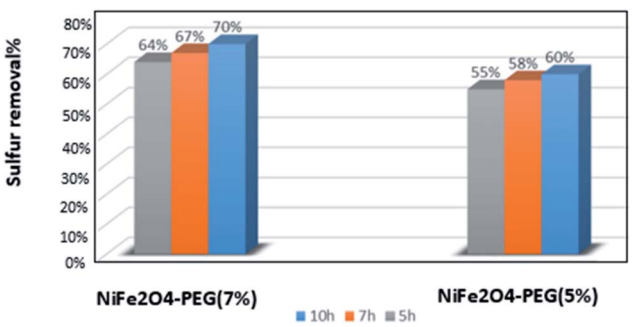

Fig. 6 Comparison between the performance of $NiFe_2O_4$–PEG with different cases of PEG and different synthesis times.

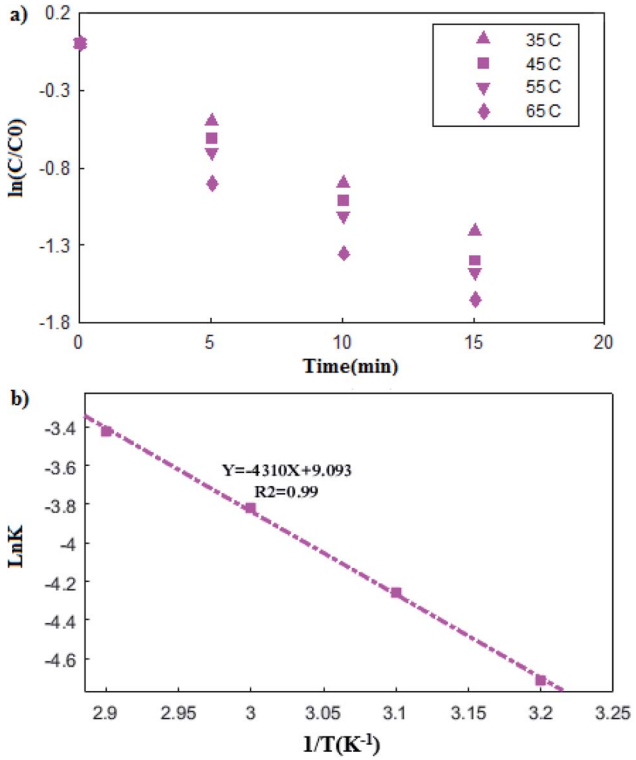

Fig. 7 (a) The plot of ln c/c_0 *versus* time at different temperature, (b) Arrhenius plot (b).

3.3. Kinetics of the DBT oxidation reaction

To describe the kinetics of the oxidation reaction of DBT, the pseudo-first-order equation was used in the temperatures range

Table 3 Thermodynamic parameters for removal of DBT from model fuel in UAOD process

Temperature (K)	K (Arrhenius constant)	ΔH° (kJ mol^{-1})	ΔG° (kJ mol^{-1})	ΔS° (kJ mol^{-1} K^{-1})
308	0.0090	33.26	85.62	−0.170
318	0.0140	33.18	88.83	−0.175
328	0.0218	33.10	90.82	−0.176
338	0.0324	33.01	92.70	−0.177

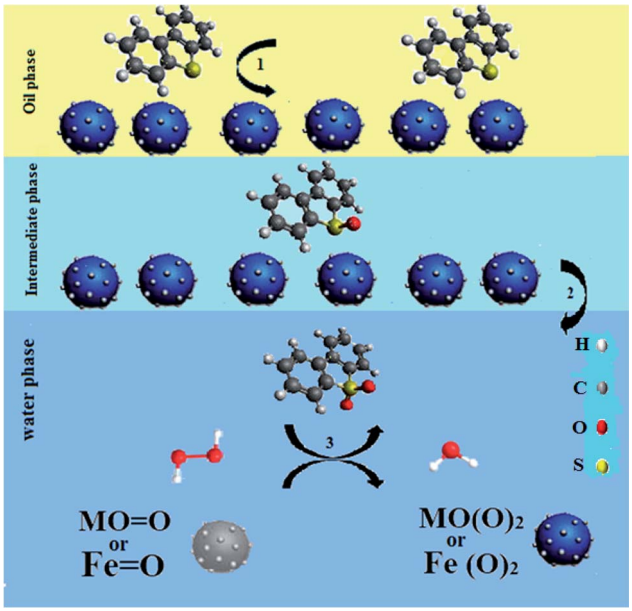

Fig. 8 Schematic illustration of the probable mechanism for the oxidation sulfur containing compounds.

of 35 to 65 °C in the UAOD process. The pseudo-first-order kinetic models are described by eqn (3):

$$\ln\left(\frac{C}{C_0}\right) = Kt \tag{3}$$

In which C_0 and C (ppm) are the sulfur concentrations at initial and time t (min), respectively. A straight line of $\ln(C/C_0)$ *vs.* t was employed to calculate K (L min^{-1}) (Fig. 7(a)). In addition, the correlation coefficients (R^2) obtained was close to one. Therefore, according to these result, the experimental data well fit pseudo-first-order model.[33–35]

3.3.1. Arrhenius (kinetic) and thermodynamic analysis. Arrhenius analysis was carried out using pseudo-first-order kinetic constants at different temperatures. The Arrhenius equation is shown by eqn (4):

$$K = Ae^{\frac{-E_a}{RT}} \tag{4}$$

In which T and R are the reaction temperature and universal gas constant, respectively. Furthermore, E_a represents the activation energy, which can be obtained by plotting the ln K, *vs.* $1/T$ (Fig. 7(b)), leading to E_a of 35.86 kJ mol^{-1}.[36] In addition, the presence of metal ions and ultrasound in the reaction system has caused relatively low activation energy.[37]

Eyring equation could be used to obtain the thermodynamic parameters of the oxidative desulfurization process:

$$\ln\frac{K}{T} = -\frac{\Delta H}{R}\frac{1}{T} + \ln\frac{K_b}{h} + \frac{\Delta S}{R} \tag{5}$$

$$\Delta H = E_a - RT \tag{6}$$

$$\Delta G = \Delta H - T\Delta S \tag{7}$$

Table 4 The 2^2 response surface design

Experimental run	Oxidant amount (mL)	Irradiation time (min)	Catalyst dose (mg)	Ultrasonic power (kHz)	Desulfurization rate (%)
1	15	10	0.10	50	73.5
1	15	10	0.10	50	73.5
2	15	15	0.05	70	65.5
3	10	10	0.10	50	39.5
4	10	5	0.10	50	40.0
5	5	10	0.15	50	50.0
6	10	5	0.05	70	58.5
7	15	15	0.05	30	52.5
8	5	5	0.15	70	72.5
9	5	15	0.05	70	46.5
10	5	5	0.05	30	22.5
11	10	15	0.15	30	66.0
12	10	10	0.10	50	32.0
13	5	15	0.05	30	30.0
14	5	5	0.05	30	42.5
15	15	10	0.10	70	66.5
16	15	5	0.05	70	29.5
17	15	10	0.10	30	35.0
18	15	15	0.15	30	40.0
19	5	15	0.10	50	40.0
20	5	10	0.05	50	31.5
21	10	5	0.15	70	45.0
22	5	5	0.15	30	60.5
23	15	15	0.15	70	82.5
24	10	15	0.15	70	50.0
25	15	5	0.15	30	36.0

Table 5 Estimated regression coefficient for the model

Source	Sum of squares	Degrees of freedom	Mean square	*F*-Value	*P*-Value
Model	5736.57	14	409.75	29.59	0001.0>
Irradiation time-X_1	242	1	242.06	5.60	0.040
X_2-Oxidant amount	3068.06	1	3068.06	70.96	0001.0>
Catalyst dose-X_3	847.35	1	847.35	19.60	0.001
Ultrasonic power-X_4	960.68	1	960.68	3.18	0.001
X_1^2	20.81	1	71.22	1.65	0.228
X_2^2	428.43	1	320.14	7.40	0.022
X_3^2	25.52	1	52.45	1.21	0.297
X_4^2	75.97	1	75.97	0.26	0.214
X_1X_2	70.06	1	0.06	0	0.970
X_1X_3	18.06	1	18.06	0.42	0.533
X_1X_4	9.00	1	9.00	0.21	0.658
X_2X_3	25.00	1	25.00	0.58	0.465
X_2X_4	4.06	1	14.06	0.33	0.581
X_3X_4	1.56	1	1.25	0.04	0.853
Residual error	432.37	10	43.24		
Total	6168.94	24			

where h and K_b are Planck and Boltzmann constants, respectively. Arrhenius analysis results were used to determine ΔH°, ΔG° and ΔS° thermodynamic parameters. The Arrhenius and thermodynamic parameters of the UAOD process at various temperatures are summarized in Table 3. As observed in the table, the values of K increase with increasing temperature. Additionally, positive values of ΔG° indicate that the oxidation reaction of DBT is non-spontaneous. Increasing the ΔG° values with increasing temperature indicates that higher temperatures improve the reaction. Positive ΔH° values have been obtained

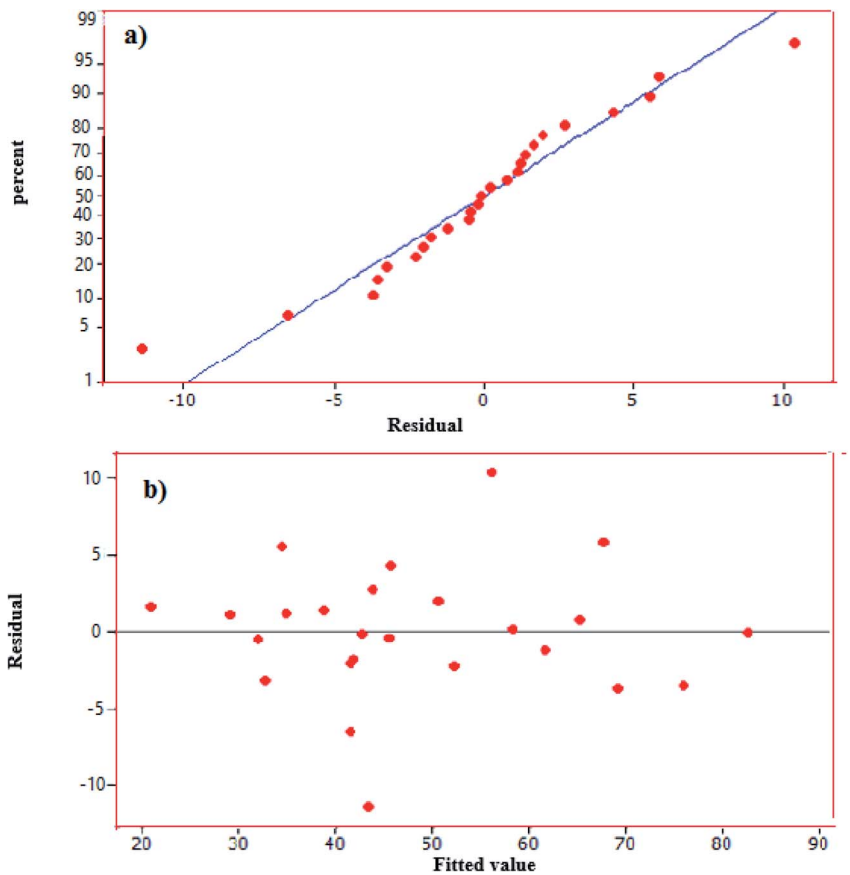

Fig. 9 (a) Normal probability plot of residuals, (b) plot of residual *versus* predicted values.

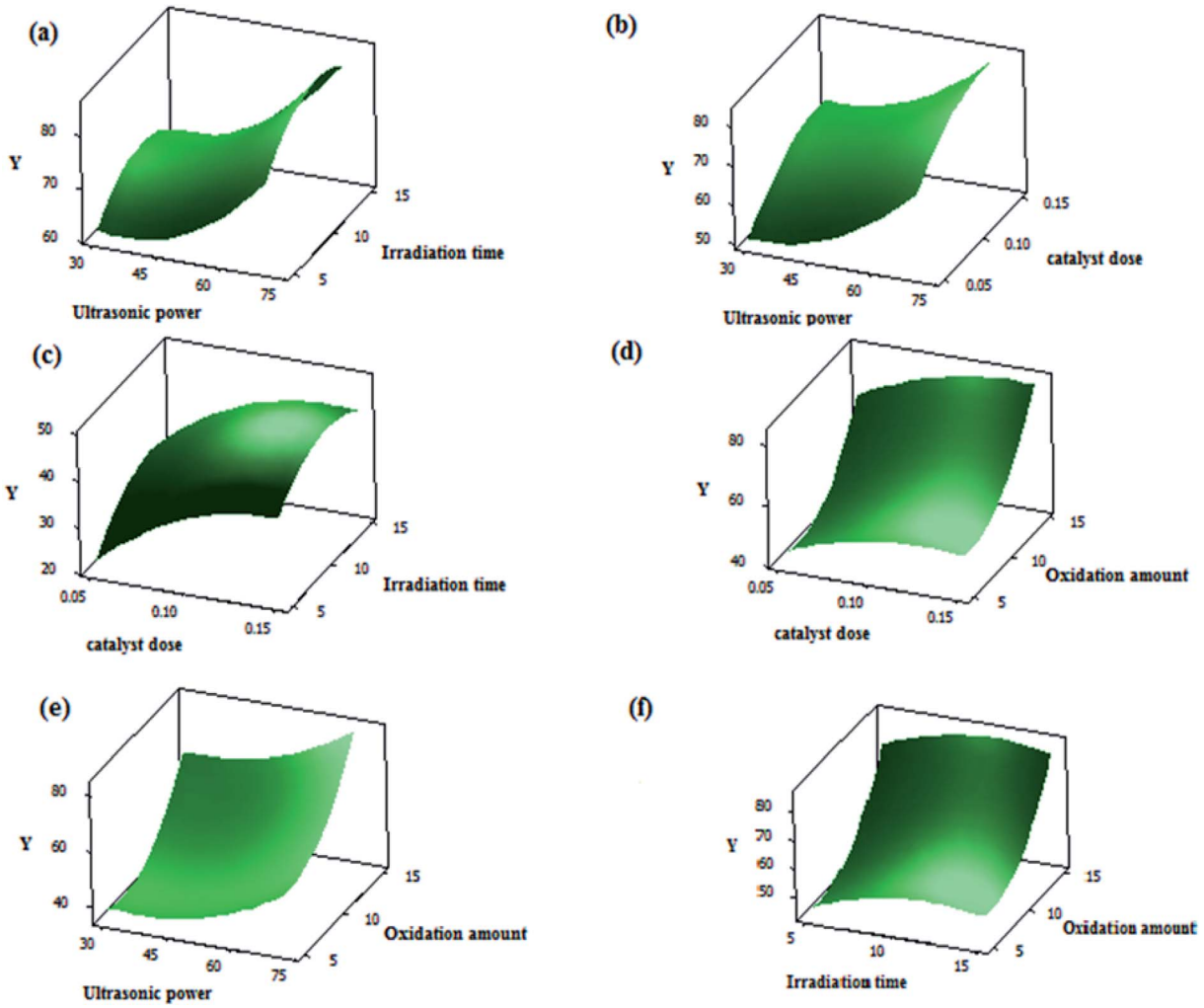

Fig. 10 (a) 3-D plot of conversion *vs.* ultrasonic power and irradiation time, (b) 3-D plot of conversion *vs.* ultrasonic power and catalyst dose, (c) 3-D plot of conversion *vs.* catalyst dose and irradiation time, (d) 3-D plot of conversion *vs.* catalyst dose and oxidation amount, (e) 3-D plot of conversion *vs.* oxidant amount and ultrasonic power, (f) 3-D plot of conversion *vs.* oxidant amount and irradiation time.

for the oxidation reaction of DBT, indicating that the process is endothermic. Negative values of ΔS indicate a decrease in stochasticity as a result of the oxidation reaction.

3.4. Proposed mechanism of UAOD oxidation reaction

In the UAOD system containing metal catalysts, PTA and heat, hydrogen peroxide is converted to hydroxyl free radicals. The hydroxyl free radicals then form superoxide. Afterwards, terminal metal atoms (M = Ni or Fe) in the $NiFe_2O_4$–PEG accept active oxygen from superoxide and Fe^{2+} is readily oxidized into Fe^{3+}, which reacts with DBT molecules, leading to sulfones.[38] The PEG present in the nanocatalyst acts as the PTA and increases the mass transfer at the interface, thus facilitating the transfer of peroxo-metal anions into the oil phase.[39] The transient cavitation, ultrasound, and PTA effective interphase transport of the oxidant were produced synergistically affect influence of fine emulsification, which leads to approximately thorough removal of DBT from the model oil.[40] Therefore, the character of cavitation and ultrasound in PTC assisted ultrasonic oxidative desulfurization is the physical process, which enhances DBT oxidation. The mechanism described in Fig. 8 is shown.

3.5. Optimization of UAOD parameters

In order to optimization the UAOD operating conditions, the effect of four parameters (*i.e.*, catalyst dose, oxidant amount, irradiation time and ultrasonic power) on the sulfur removal percentage were studied by employing the CCD method. In Table 4 are presented the runs of the experiments and the response values for each test. Based on the CCD, the regression equation to describe a mathematical correlation between the sulfur removal percentage (Y) and the selected parameters (*i.e.*, X_1, X_2, X_3 and X_4) is expressed by the following second-order polynomial equation:[41,42]

$$\text{DBT removal (\%)} = 43.3898 + 3.6667X_1 + 13.0556X_2 + 6.8611X_3 + 7.3056X_4 - 5.2881X_{12} + 11.2119X_{22} - 4.5381X_{32} - 0.0625X_1X_2 - 1.0625X_1X_3 + 0.75X_1X_4 + 1.25X_2X_3 + 0.9375X_2X_4 - 0.3125X_3X_4 \quad (8)$$

According to eqn (8), negative signs show antagonistic effects whiles positive ones indicate synergistic effects. Moreover, Table 5 presents the result of analysis of variance (ANOVA) obtained by this study. This table gives linear terms of the four variables (*i.e.*, X_1, X_2, X_3 and X_4) are statistically significant ($p < 0.05$). The results showed the coefficient of determination of $R^2 = 0.93$ represents a favorable value for model validation. Also, from the *F*-value of the model (29.59) in the ANOVA table, it can be inferred that the model is significant and it is evident that catalyst dose and oxidant amount are the most important factors in the proposed correlation (*e.g.* eqn (8)). It can be concluded that oxidant amount is the most effective parameter on the removal efficiency of DBT. Furthermore, Fig. 9(a) displays the normal probability plot of residuals used to examine the normal distribution of standard deviations. As shown, the majority of residuals follow a straight line with minimal variations from their directions. In addition, Fig. 9(b) depicts the plot of the predicted responses against residuals. Based on the data, all the points in the experimental runs are randomly distributed around the average of the response variable, indicating that the proposed model is sufficient.

3.6. Response surface and contour plots

Three dimensional (3D) surface and (2D) contour plots are the graphs, which can be used to investigate the interactive effects of the selected factors on the oxidation reaction of DBT in UAOD process. The resulted surface response 3-D plots of conversion

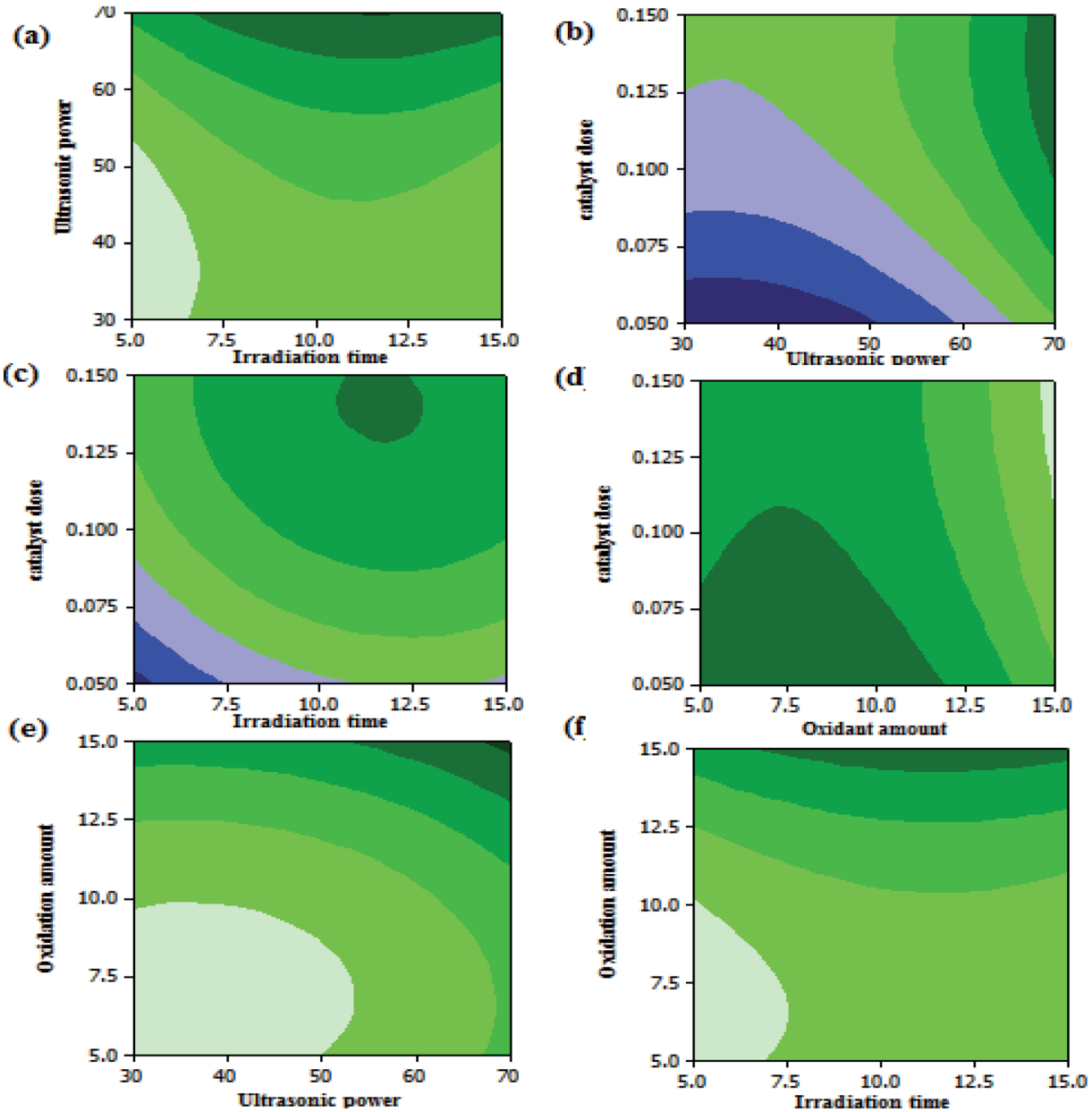

Fig. 11 (a) contour plots of ultrasonic power *vs.* irradiation time, (b) ultrasonic power and catalyst dose, (c) catalyst dose *vs.* irradiation time, (d) catalyst dose *vs.* oxidant amount , (e) oxidation amount *vs.* ultrasonic power (f) oxidant amount *vs.* irradiation time.

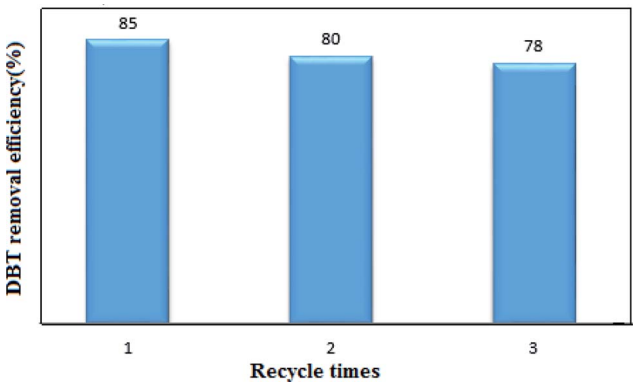

Fig. 12 Recyclability performance of nanocatalyst in UAOD of DBT.

as a function of two independent variables, (a) X_4 and X_1; (b) X_4 and X_3; (c) X_3 and X_1; (d) X_3 and X_2; (e) X_2 and X_4; (f) X_2 and X_1 are shown in Fig. 10(a–f) respectively. Also, the 2-D contour plots are shown in Fig. 11(a–f). According to surface and contour plots, the DBT removal efficiency was set to be maximum while ultrasonic power and oxidant amount dose were set at the maximum value and the other parameters were kept in range. It was also discovered that when ultrasonic power, irradiation time, oxidant amount and catalyst dose were set to 70 MHz, 11.96 min, 15 mL, and 0.14 g respectively, the maximum conversion reached 85.5%.

3.7. Regeneration experiments

Phase transfer catalyst regeneration is a significant parameter for industrial applications. The nanocatalyst selected from Fig. 6 was used in the recovery experiments. 0.15 gr of the nanocatalyst and 15 mL of H_2O_2 were used per 15 mL of the model fuel (DBT and *n*-hexane) in the UAOD process. The catalyst was removed from the reaction mixture by filtration, washed with ethanol, and finally dried at 90 °C for 1 hour. As shown in Fig. 12, after three regeneration cycles, the conversion rate of DBT has decreased from 85% to 78%, which could be due to the deposition of the produced sulfone on the nanocatalyst active sites, which results in a decrease in the catalyst activity.[43,44,46]

4. Conclusions

Efficient AFe_2O_4–PEG nanocatalysts were synthesized by hydrothermal method and the effect of different concentrations of PEG (5% and 7%) and various synthesis times were investigated. The nanocatalyst was then used in the UAOD process for the removal of DBT from a model fuel. According to the results, $NiFe_2O_4$–PEG was prepared with 7 wt% of PEG and 10 hour hydrothermal times demonstrated the best performance in comparison to other nanocatalysts. Furthermore, based on the experimental design, the optimal conditions for the UAOD process were nanocatalyst dose of 0.14 gr, irradiation time of 11.96 min, ultrasonic power of 70 MHz, and oxidant amount of 15 mL. The kinetic data show that the pseudo-first order model best describes the oxidation reaction of DBT in the UAOD process. Moreover, based on the results of the thermodynamic studies for determining the entropy, enthalpy and Gibbs free energy, the oxidation of DBT is an exothermic and non-spontaneous reaction. From Arrhenius analysis, the activation energy was obtained as 35.86 kJ mol^{-1}. In addition, the results confirmed that the increase in temperature led to the considerable improvement of the removal efficiency. However, selecting a suitable PTC is regarded an essential challenge in the UAOD process. The present nanocatalyst can be a good candidate for the removal of other sulfur compounds. The present approach, which is based on the application of mild operating conditions, high DBT conversion, and a simple mechanism, can be further developed for the industrial desulfurization of hydrocarbon fuels.

Conflicts of interest

The authors of this manuscript declare that they have no conflict of interest.

Acknowledgements

The authors acknowledge the University of Kashan by Grant No. (159271/SMT3), Semnan University and Iran National Science Foundation (INSF, 97017837) for supporting this investigation.

References

1 C. Malins, E. Dumitrescu, D. Kodjak, R. de Jong, S. Galarza, J. Akumu and B. Fabian, *Report*, 2016.
2 H. Li, W. Zhu, S. Zhu, J. Xia, Y. Chang, W. Jiang, M. Zhang, Y. Zhou and H. Li, *AIChE J.*, 2016, **62**, 2087–2100.
3 D. Zhang, H. Tao, C. Yao and Z. Sun, *Chem. Eng. Sci.*, 2017, **174**, 203–221.
4 L. Dong, G. Miao, X. Ren, N. Liao, A. W. Anjum, Z. Li and J. Xiao, *Ind. Eng. Chem. Res.*, 2020, **59**, 10130–10141.
5 J. Zou, Y. Lin, S. Wu, M. Wu and C. Yang, *Sep. Purif. Technol.*, 2021, **264**, 118434.
6 J. Zou, Y. Lin, S. Wu, Y. Zhong and C. Yang, *Adv. Funct. Mater.*, 2021, **31**, 2100442.
7 W. N. W. Abdullah, W. A. W. A. Bakar, R. Ali, W. N. A. W. Mokhtar and M. F. Omar, *J. Cleaner Prod.*, 2017, **162**, 1455–1464.
8 M. d. C. Capel-Sanchez, P. Perez-Presas, J. M. Campos-Martin and J. Fierro, *Catal. Today*, 2010, **157**, 390–396.
9 J. M. Campos-Martin, M. Capel-Sanchez, P. Perez-Presas and J. Fierro, *J. Chem. Technol. Biotechnol.*, 2010, **85**, 879–890.
10 C. Song and X. Ma, *Appl. Catal., B*, 2003, **41**, 207–238.
11 A. W. Bhutto, R. Abro, S. Gao, T. Abbas, X. Chen and G. Yu, *J. Taiwan Inst. Chem. Eng.*, 2016, **62**, 84–97.
12 A. M. Dehkordi, M. A. Sobati and M. A. Nazem, *Chin. J. Chem. Eng.*, 2009, **17**, 869–874.
13 Y. Dai, Y. Qi, D. Zhao and H. Zhang, *Fuel Process. Technol.*, 2008, **89**, 927–932.
14 J. Behin and N. Farhadian, *Ultrason. Sonochem.*, 2017, **38**, 50–61.
15 H. Lü, J. Gao, Z. Jiang, Y. Yang, B. Song and C. Li, *Chem. Commun.*, 2007, 150–152.

16 F. M. Collins, A. R. Lucy and C. Sharp, *J. Mol. Catal. A: Chem.*, 1997, **117**, 397–403.
17 A. E. S. Choi, S. Roces, N. Dugos, C. M. Futalan, S.-S. Lin and M.-W. Wan, *J. Taiwan Inst. Chem. Eng.*, 2014, **45**, 2935–2942.
18 L. Thompson, Science and engineering, *Ind. Eng. Chem. Res.*, 1999, **38**, 1215–1249.
19 J.-L. Luche, *Synthetic organic sonochemistry*, Springer Science & Business Media, 2013.
20 Y. T. Shah, A. Pandit and V. Moholkar, *Cavitation reaction engineering*, Springer Science & Business Media, 1999.
21 K. Keynejad, M. Nikazar and B. Dabir, *Pet. Sci. Technol.*, 2018, **36**, 718–725.
22 L. Doraiswamy, in *Organic Synthesis Engineering*, Oxford University Press, 2001.
23 T. Sachdeva and K. Pant, *Fuel Process. Technol.*, 2010, **91**, 1133–1138.
24 J. Qiu, G. Wang, D. Zeng, Y. Tang, M. Wang and Y. Li, *Fuel Process. Technol.*, 2009, **90**, 1538–1542.
25 J. Li, Z. Yang, S. Li, Q. Jin and J. Zhao, *J. Ind. Eng. Chem.*, 2020, **82**, 1–16.
26 D. S. Zhao, Z. M. Sun, F. T. Li and H. D. Shan, *J. Fuel Chem. Technol.*, 2009, **37**, 194–198.
27 Y. Köseoğlu, M. Bay, M. Tan, A. Baykal, H. Sözeri, R. Topkaya and N. Akdoğan, *J. Nanopart. Res.*, 2011, **13**, 2235–2244.
28 H. A. H. Alshamsi and S. H. Alwan, *Res. J. Pharm., Biol. Chem. Sci.*, 2015, **6**, 985–996.
29 N. Hussain, S. Alwan, H. Alshamsi and I. Sahib, *Int. J. Chem. Eng.*, 2020, **2020**, 9068358.
30 B. Davodi, M. Jahangiri and M. Ghorbani, *Particulate Science and Technology*, 2020, **38**(3), 325–336.
31 Z. J. Zhang, X. Y. Chen, B. N. Wang and C. W. Shi, *J. Cryst. Growth*, 2008, **310**, 5453–5457.
32 Y. Xiaotun, X. Lingge, N. S. Choon and C. S. O. Hardy, *Nanotechnology*, 2003, **14**, 624.
33 H. Altaee, H. A. H. Alshamsi and B. A. Joda, *AIP Conf. Proc.*, 2020, **2290**, 030036.
34 H. Altaee and H. A. Alshamsi, *J. Phys.: Conf. Ser.*, 2020, **1664**, 012074.
35 N. Jose, S. Sengupta and J. Basu, *Fuel*, 2011, **90**, 626–632.
36 V. Garshasbi, M. Jahangiri and M. Anbia, *Appl. Surf. Sci.*, 2017, **393**, 225–233.
37 Y. Dai, D. Zhao and Y. Qi, *Ultrason. Sonochem.*, 2011, **18**, 264–268.
38 H. Mei, B. Mei and T. F. Yen, *Fuel*, 2003, **82**, 405–414.
39 M. A. Rezvani, S. Khandan and N. Sabahi, *Energy Fuels*, 2017, **31**, 5472–5481.
40 J. B. Bhasarkar, M. Singh and V. S. Moholkar, *RSC Adv.*, 2015, **5**, 102953–102964.
41 M. Alimohammady, M. Jahangiri, F. Kiani and H. Tahermansouri, *Res. Chem. Intermed.*, 2018, **44**(1), 69–92.
42 H. A. Alshamsi, M. A. Al Bedairy and S. H. Alwan, *IOP Conf. Ser. Earth Environ. Sci.*, 2021, **722**, 012005.
43 M. A. Rezvani, Z. Shokri Aghbolagh, H. Hosseini Monfared and S. Khandan, *J. Ind. Eng. Chem.*, 2017, **52**, 42–50.
44 M. A. Al-Bedairy and H. A. H. Alshamsi, *Eurasian J. Anal. Chem.*, 2018, **13**(6), em72.
45 T. O. Sachdeva and K. K. Pant, *Fuel Process. Technol.*, 2010, **91**, 1133–1138.
46 F. Vafaee, S. Mandizadeh, O. Amiri, M. Jahangiri and M. Salavati-Niasari, *RSC Adv.*, 2021, **11**, 22661–22676.
47 T.-C. Chen, Y.-H. Shen, W.-J. Lee, C.-C. Lin and M.-W. Wan, *J. Cleaner Prod.*, 2010, **18**, 1850–1858.
48 M.-W. Wan and T.-F. Yen, *Appl. Catal., A*, 2007, **319**, 237–245.
49 M. A. Rezvani, M. Shaterian, F. Akbarzadeh and S. Khandan, *Chem. Eng. J.*, 2018, **333**, 537–544.
50 C. Zhou, Y. Wang, X. Huang, Y. Wu and J. Chen, *Chem. Eng. Process.*, 2020, **147**, 107789.
51 I. Najafi, M. A. Makarem and M. Amani, *Adv. Pet. Explor. Dev.*, 2011, **2**, 63–69.